Check for updates

Advanced Functional Materials

ADVANCED FUNCTIONAL MATERIALS
www.afm-journal.de

RESEARCH ARTICLE OPEN ACCESS

Tailoring Light Management in All-Perovskite Tandem Solar Cells: The Impact of Nanotextures

Sebastian Berwig[1] | Yeonghun Yun[1] | Doyun Im[1,2] | Isabella Taupitz[1] | Alexandros Cruz[1] | Marlene Härtel[1] | Bor Li[1] | Kevin J. Prince[1] | Hanifah Winarto[1] | Thomas W. Gries[1] | Klaus Jäger[1] | Florian Riesebeck[1] | Daniele Mantione[3,4,5] | Sharon Monaci[3,4] | Silvia Mariotti[1] | Vishnu Vijayakumar[6] | René A. J. Janssen[6] | Sangwook Lee[2] | Bernd Stannowski[1,7] | Christiane Becker[1,8] | Philipp Tockhorn[1] | Steve Albrecht[1,9]

[1]Solar Energy Division, Helmholtz-Zentrum Berlin für Materialien und Energie GmbH, Berlin, Germany | [2]School of Materials Science and Engineering, Kyungpook National University (KNU), Daegu, Republic of Korea | [3]POLYMAT, University of the Basque Country, Donostia/San Sebastián, Spain | [4]POLYKEY POLYMERS S.L., Donostia/San Sebastián, Spain | [5]IKERBASQUE, Basque Foundation for Science, Bilbao, Spain | [6]Molecular Materials and Nanosystems & Institute for Complex Molecular Systems, Eindhoven University of Technology, Eindhoven, The Netherlands | [7]Berliner Hochschule für Technik, Berlin, Germany | [8]Hochschule für Technik und Wirtschaft Berlin, Berlin, Germany | [9]Fakultät IV – Elektrotechnik und Informatik, Technische Universität Berlin, Berlin, Germany

Correspondence: Steve Albrecht (steve.albrecht@helmholtz-berlin.de)

Received: 29 May 2026 | **Revised:** 6 August 2026 | **Accepted:** 10 August 2026

Keywords: all-perovskite tandem solar cells | light management | nanotextures | optical performance | optical simulations

ABSTRACT

All-perovskite tandem solar cells (APTSCs) emerge as promising low-cost and high-efficiency next-generation photovoltaics. To further increase the power conversion efficiencies (PCEs), a deeper understanding and fine-tuned optimization of the optics is required, since most reports fall below 90% of the theoretical limit in photocurrent. Here, we demonstrate a synergistic multi-faceted approach to overcome the optical constraints: incorporation of front-sided nanotextures into APTSCs yields a broadband improvement of light in-coupling, which eliminates thin-film interference effects in reflectance, equivalent to a gain of 0.45 mA•cm^{-2} in photocurrent. On the material level, parasitic absorption is reduced by optimizing the front ITO layer and replacing PEDOT:PSS for the bottom subcell with a graphene oxide/self-assembled monolayer (GO/SAM) bilayer, improving the overall current gain to 1 mA•cm^{-2} in each subcell. The resulting APTSC achieves a power conversion efficiency (PCE) of 27.98% with a short-circuit current density (J_{SC}) of 17.18 mA•cm^{-2}, one of the highest reported values for this technology to date. Through comprehensive optical simulations, we explore the optical potential of APTSCs and further highlight upper limits of the subcell photocurrents in various tandem architectures. This work provides experimental and theoretical insights into optical optimization routes to increase the PCE of APTSCs well beyond 30%.

1 | Introduction

All-perovskite tandem solar cells (APTSCs) are a proven concept to enable power conversion efficiencies (PCEs) beyond the thermodynamic limit of single-junction solar cells while offering low-temperature processing, use of cost-effective materials, and advantages of thin-film technologies [1]. The use of a wide bandgap (WBG) mixed halide and narrow bandgap (NBG) Sn-Pb perovskite as top and bottom subcell absorbers, respectively, enabled a rise in PCE up to certified 30.3% [2]. This rise in PCE was mainly driven by interfacial engineering, i.e., passivating surface and interfacial defects and tuning energy levels to

This is an open access article under the terms of the Creative Commons Attribution License, which permits use, distribution and reproduction in any medium, provided the original work is properly cited.
© 2026 The Author(s). *Advanced Functional Materials* published by Wiley-VCH GmbH

minimize non-radiative losses [3–5]. Additionally, improvements in the NBG bulk properties by inhibiting the facile Sn(II) oxidation [6], balancing the crystallization in mixed Sn-Pb systems [7], or passivating grain boundary defects by adding organic salts [8] led to higher PCEs in APTSCs as well.

However, optical improvements of the APTSCs layer stack have been reported rarely. Foremost, the replacement of the parasitically absorbing PEDOT:PSS hole transport layer (HTL) has been investigated before by the usage of self-assembled monolayers [9–11], novel metal oxides [12] or polymers [13]. While these strategies improved the photocurrent generation in the bottom cell by up to 0.5 mA•cm^{-2}, they are limited by the light in-coupling of the stack. The introduction of light management strategies such as moth-eye antireflective coatings [14] or fluorinated tin oxide (FTO) nanoplatelets for a nanoscale random texture [15] has shown enhancements to the J_{SC} of APTSCs. Nevertheless, these strategies are inflexible and still fall short of 90% of the theoretical limit of photocurrent [16]. Here, the photocurrent density limit is based on an integration of the AM1.5G spectrum over all energies ≥ 1.25 eV, i.e., the bandgap of the bottom subcell with a step-like absorption. To surpass this threshold, a multi-faceted approach is required, which targets highly parasitically absorbing layers within APTSCs and utilizes advanced light management structures.

Recently, we investigated the incorporation of sinusoidal nanotextures in APTSCs numerically [17] and reported that front-side integration of nanotextures between glass and transparent conductive oxide (TCO) front electrode can improve the matched photogenerated current density by 0.42 to 0.75 mA•cm^{-2}, for a texture aspect ratio between 27% and 54%. In this work, we expand on our theoretical findings and incorporate front-sided, sinusoidal nanotextures into high-performance APTSCs. We prove experimentally that such sinusoidal nanotextures induce a broadband reduction of reflection losses. We examine the structural, morphological, and opto-electronic properties of the wide bandgap (WBG) subcell fabricated atop the nanotextures and demonstrate that the WBG quality is unaffected. Additionally, we tailor a high-temperature indium tin oxide (ITO) sputtering process for the front contact in APTSCs. Guided by optical and electrical simulations, we developed a thin, highly doped ITO layer that maximizes transparency while minimizing series resistance losses.

Furthermore, we evaluated the replacement of PEDOT:PSS with a self-assembled molecule (SAM) based bilayer optically. Ultimately, our optically optimized tandem stack resulted in a PCE of 27.98% with a matched J_{SC} of 17.18 mA•cm^{-2}, which stands amongst the highest reported values for this technology and surpasses 90% of the theoretical photocurrent limit. Lastly, we deliver an outlook for the optical performance of APTSCs via optical simulations, assuming processability of 20 µm thick Sn-Pb perovskites on micron-sized textures. We show that for planar interconnecting layers, index matching becomes crucial for efficient light transmission through SnO_x into the bottom subcell, while texturing the interconnecting layers between subcells alleviates this dependency. A comparison between superstrate and substrate configuration reveals that optically, the latter heavily relies on material alternatives to C_{60}. Employing 20 µm thick single-crystal Sn-Pb perovskites emerges as a promising choice for light absorption, especially when combined with micron-sized textures.

2 | Results and Discussion

2.1 | Implementation of Nanotextures

To contextualize the above-discussed optical trends in APTSCs, we analyzed recent reports of APTSCs and perovskite silicon tandem solar cells (PSiTSCs) regarding their optical performance. For this, we evaluated reported tandem external quantum efficiency (EQE) and reflectance spectra and put the (equivalent) photocurrent densities into perspective against an upper limit. A detailed description of the process is given in Table S1. In Figure 1a the mean values of the spectrally integrated equivalent photocurrent densities of bottom and top cell absorption, as well as reflectance and internal losses (sum of parasitic absorption and charge collection losses defined as the difference between EQE and 1−reflectance) from nine representative publications for either technology (references provided in Table S1) are shown as absolute values of the (equivalent) photocurrent densities (left panel) and respective fractions with respect to the upper limit (right panel). Compared to PSiTSCs, in APTSCs the portions of the subcell absorption are lower for the mean values due to higher reflectance and internal losses. This trend also holds true when comparing the best reported values (Figure S2), highlighting the need for optical optimization in APTSCs to further advance this technology. Internal losses in APTSCs can originate from parasitic absorption in contact layers, e.g., the front ITO and the recombination layer, as well as the prevalent PEDOT:PSS as HTL for the bottom subcell [16]. In PSiTSCs, parasitic absorption mostly stems from the front-facing contact layers, i.e., the front TCO, SnO_x, and C_{60}. On the other hand, APTSCs suffer severely from high reflectance losses due to the state-of-the-art planar architecture, while for PSiTSCs, significant efforts have been taken to implement nano [18], sub-micron [18, 19] or micron-sized [20] textures into the perovskite top cell to suppress interfacial reflection [21] and enhance band edge absorption in silicon [22].

In planar APTSCs, reflection losses are dominated by Fresnel reflections at interfaces and thin-film interferences over the whole spectral range, severely limiting the spectral response of both WBG and NBG subcells. In this study, we investigate whether incorporating sinusoidal nanotextures (pitch 720 nm, height 370 nm) at the front side of the tandem stack can suppress these reflection losses. Figure 1b shows a scanning electron microscopy (SEM) cross-section image and corresponding schematic layer stack of an APTSC on nanotextures. A comparison with a planar counterpart is displayed in Figure S3. We fabricated nanotextures by nanoimprint lithography (details of the fabrication process in Figure S4 and methods section) and chose sinusoidal nanotextures, since they outperform other geometries and are well compatible with solution processing of SAMs and perovskite absorbers [23]. After fabricating the nanotextures on glass substrates, we deposited a highly doped ITO layer by dc-sputtering at substrate temperatures of approximately 300°C. The opto-electrical trade-off during a thickness variation was calculated and optimized via optical simulations with GenPro4 [24] and electrical simulations with Quokka3 [25] (further details in the methods section, Note S1 and Figure S5).

16163028, 2026, 76, Downloaded from https://advanced.onlinelibrary.wiley.com/doi/10.1002/adfm.77815 by Helmholtz-Zentrum Berlin Für, Wiley Online Library on [10/11/2026]. See the Terms and Conditions (https://onlinelibrary.wiley.com/terms-and-conditions) on Wiley Online Library for rules of use; OA articles are governed by the applicable Creative Commons License

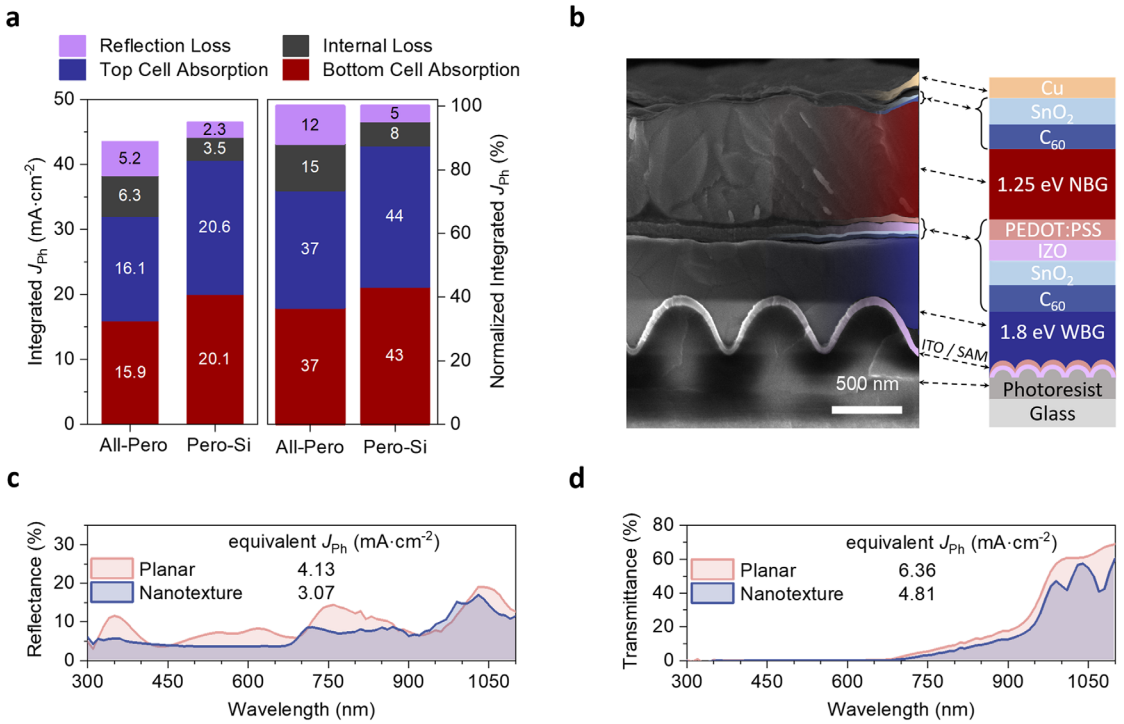


FIGURE 1 | (a) Mean optical performance of nine reported all-perovskite tandem solar cells (APTSCs) and perovskite-silicon tandem solar cells (PSiTSCs). The left panel shows the (equivalent) photocurrent density generated in the top and bottom subcells and lost internally or in reflection for either technology. Note that the different bottom subcell bandgaps result in different current density sums. The right panel shows the respective fractions of the theoretically achievable current density for both architectures. A detailed description of the analysis procedure and the list of literature references is provided in Table S1 and Figure S1. (b) SEM cross-section view and corresponding schematic APTSC layer stack on a nanotextured substrate. (c) Reflectance and (d) transmittance spectra of APTSCs stacks without Cu back contact on planar and nanotextured substrates.

APTSCs are then fabricated following the layer stack sequence of glass/textured photoresist/ITO/SAM/WBG/C_{60}/SnO_x/IZO/PEDOT:PSS/NBG/C60/SnO_x/Cu. Here, SAM is a self-assembled monolayer comprised of (4-(3,6-diphenyl-9H-carbazol-9-yl)butyl)phosphonic acid (Ph-4PACz), WBG a 1.8 eV perovskite absorber with the composition $Cs_{0.22}FA_{0.78}Pb(I_{0.7}Br_{0.3})_3)_{0.91}(MAPbCl_3)_{0.09}$, IZO is indium zinc oxide and NBG a 1.25 eV perovskite absorber with the composition of $Cs_{0.1}FA_{0.6}MA_{0.3}Sn_{0.55}Pb_{0.45}I_3$. Details of the fabrication process are provided in the Methods section.

To assess the potential of nanotextures in APTSCs, we investigate the optical reflection and transmission (Figure 1c,d, respectively), which show lower reflection losses in the range from 300 to 1100 nm, resulting in a reduction of reflected photocurrent from 4.13 to 3.07 mA•cm^{-2}. The prevalent reflectance dips caused by thin film interference in the planar architecture are eliminated in the nanotexture stack due to the superior light in-coupling properties of the nanotextures (Figure 1c), resulting in a flatter reflectance spectrum. From transmittance measurements (Figure 1d), we observe reduced transmittance with nanotextures. In combination with the reduced reflectance, it is further evident that absorption is enhanced close to the band edge of the NBG perovskite for the nanotexture stack, confirming our previous findings, as well as literature reports [15, 17, 23]

Motivated by these optical improvements of the APTSC stack, we studied structural and optoelectronic properties of the WBG subcell when fabricated on nanotextured instead of planar substrates. From SEM top view images (Figure S6), we observe similar grain morphologies and size distribution for WBG perovskite films on planar and nanotextured substrates. Both films show formation of platelet-like features at grain boundaries, which we speculate to be residual PbI_2 [26] We conducted atomic force microscopy (AFM) measurements to quantify the surface roughness of the WBG perovskite films (Figure S7) and both the topology and calculated root mean square (RMS) surface roughness (planar: 25.9 nm; nanotextured: 25.4 nm) (Table S2) are similar between both substrates. Lastly, SEM cross-section views (Figure S8) confirm complete coverage and void-free filling of the nanotextures by the WBG film. Thus, we restrict the comparison of structural and optoelectronic properties to the WBG subcell since we can assume that from the C_{60}/ALD SnO_x interface onward, layers on nanotextured and planar substrates behave identically.

To investigate the crystalline properties of the WBG perovskite absorber, we conducted grazing incidence X-ray diffraction (GIXRD) measurements (1° angle of incidence) of ITO/SAM/WBG layer stacks on planar and nanotextured substrates, with the diffractograms shown in Figure 2a. For both substrates, the films form a cubic perovskite lattice without secondary perovskite phases. We observe a (001) PbI_2 peak (12.7°) [27] on both substrates, which we attribute to the observed platelets in SEM top-view images. The perovskite peaks do not show a significant shift between the substrates, indicating similar crystal properties. The peak area ratio of PbI_2/(100) peaks is 0.49 and 0.41 for the nanotextured and planar sample, respectively,

16163028, 2026, 76, Downloaded from https://advanced.onlinelibrary.wiley.com/doi/10.1002/adfm.77815 by Helmholtz-Zentrum Berlin Für, Wiley Online Library on [10/11/2026]. See the Terms and Conditions (https://onlinelibrary.wiley.com/terms-and-conditions) on Wiley Online Library for rules of use; OA articles are governed by the applicable Creative Commons License

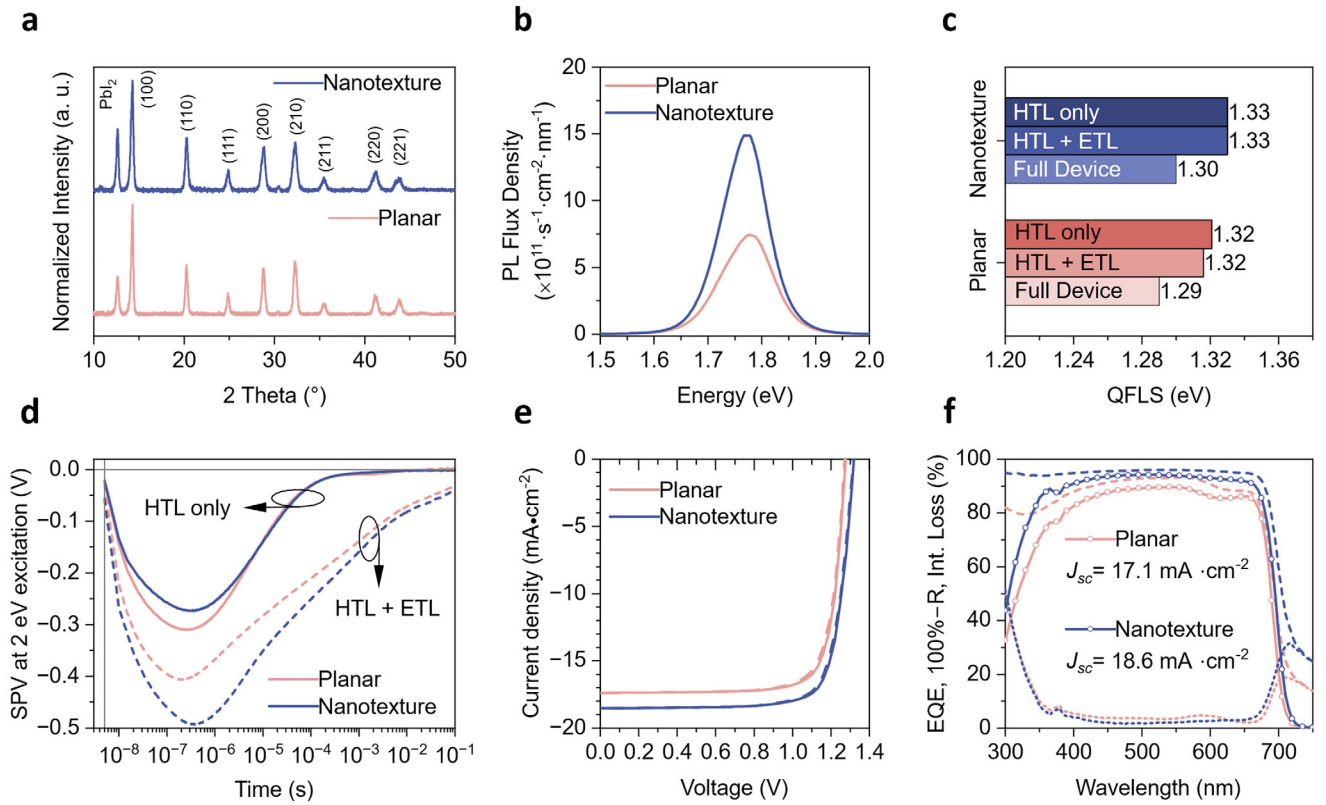


FIGURE 2 | Comparison of WBG perovskite films and single-junction solar cells on planar and nanotextured substrates. (a) X-ray diffractograms and (b) absolute photoluminescence measurements of WBG films with a layer stack ITO/SAM/WBG. (c) Layer-by-layer QFLS analysis for WBG films with first the layer stack of (a,b) ("HTL only"), then adding C_{60} ("HTL + ETL") and SnO_x/Cu ("full device"). (d) Transient surface photovoltage measurements of WBG perovskite films with HTL only and with HTL + ETL. (e) current-density/voltage (JV) and (f) EQE, 100%-Reflectance and internal loss spectra of WBG single-junction solar cells. The J_{SC} values in (f) are integrated values from the respective EQE spectrum.

indicating a higher amount of PbI_2 near the surface for the nanotextured sample. The role of residual PbI_2 in perovskite films is disputed and a topic of ongoing discussion requiring future research [28–30].

Moving forward from the structural properties, we next examine the optoelectronic properties of the WBG subcell. To pinpoint origins of non-radiative recombination, we conducted layer-by-layer absolute photoluminescence (PL) analysis on both substrates [31], where the hole transport layer (HTL) and electron transport layer (ETL) are added successively. Figure 2b displays the PL signal of bare WBG films on SAM-coated planar and nanotextured substrates. The absolute PL intensity is enhanced for the perovskite film on nanotextures, while the central peak position slightly shifts to lower energies from the planar case (1.78 eV) to the nanotextured case (1.77 eV). Such a redshift can be explained by the reciprocity relation between absorption and emission [32] and was reported for (nano-)textured silicon [33, 34] and perovskite solar cells [23]. Figure 2c shows the calculated quasi-Fermi level splitting (QFLS) from absolute PL measurements on different half stacks on planar and nanotextured substrates. For half stacks of ITO/SAM/WBG ("HTL only"), QFLS of 1.33 and 1.32 eV are measured for nanotextured and planar substrates, respectively. This indicates that the nanotextures neither compromise the optoelectronic quality of the WBG absorber nor the interfacial properties with the HTL. In contrast, the nanotextures may even slightly improve the optoelectronic properties of this half stack. The layer stacks retain their respective QFLS values after deposition of an interfacial treatment and C_{60} ("HTL + ETL"), indicating well-working passivation for both substrate types. In full devices (with atomic layer deposition, ALD), a SnO_x layer and Cu back electrode, a slight drop in QFLS can be observed for both substrates (planar: 1.29 eV; nanotextures: 1.30 eV).

To gain insights into the charge extraction dynamics, we conducted time-resolved surface photovoltage (trSPV) measurements (Figure 2d), where the initial slope of the SPV transients indicates the speed of charge extraction while the signal amplitude indicates the amount of separated charges [35, 36]. We disentangle the interface-specific contributions by measuring two different half stacks, i.e., *HTL only* and *HTL + ETL*. In the *HTL-only* case (without C_{60}), both substrates show an identical initial slope in the first 10 ns. The minima (i.e., highest SPV amplitude) are reached within a similar time (250 and 330 ns for planar and nanotextured, respectively), indicating efficient charge separation for both substrates at the HTL interface. Furthermore, we observe an absence of signal in the ms-range for both samples, indicating the absence of deep trap states [37]. This highlights SAMs as a superior choice for non-planar interfaces, as reported earlier [18, 38]

Applying C_{60} on top of the perovskite (*HTL+ETL*) enhances the charge separation. Especially in the nanotextured case, the initial SPV rise is steeper and the amplitude larger, implying faster and

16163028, 2026, 76, Downloaded from https://advanced.onlinelibrary.wiley.com/doi/10.1002/adfm.77815 by Helmholtz-Zentrum Berlin Für, Wiley Online Library on [10/11/2026]. See the Terms and Conditions (https://onlinelibrary.wiley.com/terms-and-conditions) on Wiley Online Library for rules of use; OA articles are governed by the applicable Creative Commons License

higher separation of charges. Potentially introduced deep trap states, apparent from the now present SPV signal in the ms-range, likely arise from the C_{60} interface for both planar and nanotextured samples [39].

We then fabricated WBG single-junction perovskite solar cells on planar and nanotextured substrates to evaluate the effects on devices. The JV scans (Figure 2e) of the planar WBG solar cell resulted in a J_{SC} of 17.39 mA•cm^{-2}, a V_{oc} of 1.277 V, a FF of 79.4%, and a PCE of 17.63% from the reverse scan. In contrast, the nanotexture WBG solar cell yielded a J_{SC} of 18.53 mA•cm^{-2}, a V_{OC} of 1.319 V, a FF of 78.8%, and a PCE of 19.26% from the reverse scan direction. The nanotexture-based WBG single junction greatly surpasses the planar counterpart, especially due to a higher J_{SC}. The statistical distribution of device parameters on planar and nanotextured substrates confirms the nanotextures' clear advantage in J_{SC}, at slightly higher parameter spread (Figure S9). The increase in J_{SC} from 17.39 mA•cm^{-2} on planar to 18.53 mA•cm^{-2} on nanotextured substrates is due to a broadband improvement of the EQE and reflectance (Figure 2f). The EQE of the nanotextured WBG perovskite solar cell is overall higher than the planar, driven by lower reflection losses and more efficient charge extraction, further illustrated in the corresponding internal quantum efficiency (IQE) spectra (Figure S10). Additionally, slight dips in the reflectance curve of the planar solar cell are nullified with the nanotextures, highlighting the improved light in-coupling. We note that the increased perovskite volume when using nanotextures may contribute ca. 0.5 mA/cm^2 to the gain in photocurrent (cf. Note S2 and Figure S11).

Reflection losses at the planar front-sided air/glass interface are not affected by the nanotextures, as evident from the constant reflectance offset of 3%–4% in the reflectance spectrum (Figure 2f) of the nanotexture device. In agreement with the previous results from PL, we observe a slight redshift in the absorption onset of the WBG perovskite from planar to nanotextured substrates, i.e., the inflection points of the EQE shifting from 690 nm (planar) to 695 nm (nanotextured) in Figure S12. Since the band edge slope is unaffected (Figure S12), this could be attributed to a slight bandgap reduction of the WBG perovskite when fabricated on nanotextures, although light trapping can exert similar effects in the low absorption regime close to the band edge [23]. The enhancement in V_{OC} is consistent with the PL measurements and is due to improved retention of QFLS in the absorber upon contact with C_{60}. Suns-V_{oc} measurements, i.e., V_{OC} measured at varying illumination intensity, also reveal a slightly lower ideality factor of 1.58 on nanotextures compared to 1.62 on planar substrates (Figure S13). In summary, the fabrication of WBG perovskite solar cells atop nanotextures is only minimally affected by the change in substrate topography. Importantly, we see a significant enhancement in J_{SC} and V_{OC} when transferring the processing conditions for planar substrates to nanotextured ones. While the enhanced J_{SC} can directly be referred to as enhanced light absorption, the increased V_{OC} is consistent with previous reports of perovskites fabricated on nanotextures [18, 23]. The expected gain due to the increased J_{SC} is calculated to be only 1.6 mV, indicating that the V_{OC} increase might be a result of imbalanced carrier densities and suppressed recombination [40]. Understanding the role of additional effects such as photon recycling requires dedicated studies, as pointed out in our previous publication [23]. In the next step, we integrate the nanotextures into APTSCs and analyze their effect on their optical performance in detail.

2.2 | Further Optical Optimization of APTSCs

To fabricate APTSCs on nanotextured substrates, the WBG perovskite solar cells investigated above are extended with a recombination junction of sputter-deposited IZO and a Sn-Pb NBG perovskite subcell from the SnO_x layer onward, following the layer stack depicted in Figure 1b. We aim to develop optically optimized APTSCs, which combine the nanotextures' capability of reducing reflection losses with minimized parasitic absorption losses in front of the TCO and HTL of the NBG subcell. In the following, we describe the optical optimization process of APTSCs by addressing both layers in conjunction with the front-sided nanotextures.

Starting with the front ITO layer, we reconsidered the implemented layer thickness and conducted an optoelectronic optimization for a highly doped and low-resistivity ITO layer deposited by a high-temperature sputter process in analogy to previous works [41]. We evaluated optical and series resistance losses when varying the ITO layer thickness and found that for the application in APTSCs, a reduction in thickness from 150 to 50 nm results in a net gain of PCE, due to better transmission while accepting minimal losses in series resistance (Note S1 and Figures S14 and S15). Figure 3a and b depict the EQE of the tandem solar cells and corresponding reflectance spectra for a 150 and 50 nm front ITO, respectively. The thinner front ITO shifts the thin-film interference maxima to lower wavelengths, thereby easing its effects on the reflectance spectrum. This leads to reduced reflection losses in the visible range and an increase in absorption for the top cell, increasing the integrated J_{SC} from 16.37 to 16.70 mA•cm^{-2}. At the same time, the NBG subcell benefits from lower free carrier absorption in the infrared (IR) spectral range, increasing the photogenerated current density from 15.72 to 16.58 mA•cm^{-2}. The improved photogeneration is also reflected in improved J_{SC} (150 nm ITO: 15.70 mA•cm^{-2}; 50 nm ITO: 16.43 mA•cm^{-2}) in JV curves, shown in Figure S16a, with the corresponding PV parameters listed in Table S3.

Although a thinner front TCO already boosts the current generation in both subcells, the planar architecture is still limited by thin-film interferences in the NBG regime, evoked by the WBG perovskite absorber. Therefore, we then implemented front-sided nanotextures into the APTSC (Figure 3c) with the JV curve shown in Figure S16b. Equivalent to the WBG perovskite single junction, the current generation in the top cell is greatly enhanced due to the minimized reflection losses, resulting in an increase in top cell current density from 16.70 mA•cm^{-2} in the planar stack to 17.22 mA•cm^{-2} in the nanotextured one. In the spectral range above 700 nm, the front-sided nanotextures reduce the thin-film interferences in the reflectance curve, likely evoked by their light scattering properties, and also flatten out the spectral response of the NBG subcell. Furthermore, the EQE onset is slightly redshifted compared to the planar case (Figure S17). This does not directly translate into an improved current density, as the NBG subcell on nanotextures reaches an integrated J_{SC} of 16.51 mA•cm^{-2} compared to 16.58 mA•cm^{-2} on the planar stack. Rather, we observe an increase in the internal losses in the NBG

16163028, 2026, 76, Downloaded from https://advanced.onlinelibrary.wiley.com/doi/10.1002/adfm.77815 by Helmholtz-Zentrum Berlin Für, Wiley Online Library on [10/11/2026]. See the Terms and Conditions (https://onlinelibrary.wiley.com/terms-and-conditions) on Wiley Online Library for rules of use; OA articles are governed by the applicable Creative Commons License

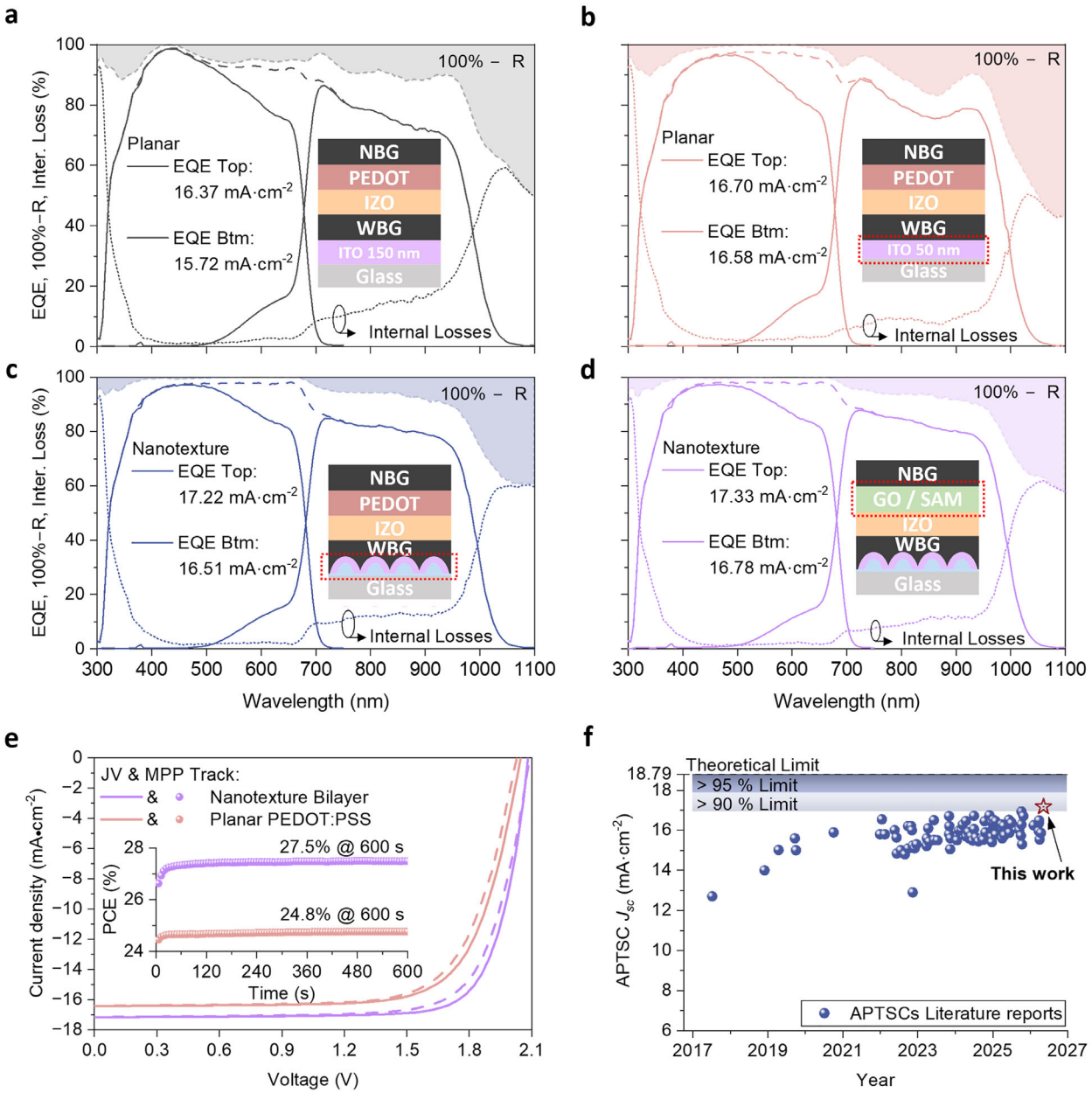


FIGURE 3 | Optical optimization of APTSCs. Tandem EQE, 100%-Reflectance and internal loss spectra of (a) Planar tandem stack with 150 nm front ITO, (b) planar stack with 50 nm front ITO, (c) nanotextured stack with 50 nm front ITO and PEDOT:PSS in NBG subcell, (d) nanotexture tandem stack with 50 nm front ITO and with graphene oxide (GO)/SAM bilayer replacing PEDOT:PSS in NBG subcell. All EQE spectra were measured with a planar anti-reflective foil at the air/glass interface. (e) Champion JV curve and maximum-power-point (MPP) tracking of a planar and the optically optimized APTSCs. The inset figures in (a–d) show the APTSC layer stack with the adapted changes highlighted. It must be noted that for improved clarity, not all functional layers of the APTSC are depicted. (f) Summary of reported J_{SC} values for 2-terminal APTSCs with the result of this work highlighted. Constraints of a tandem V_{OC} of > 1.9 V and the use of a Sn-Pb perovskite in the bottom subcell were set to select the data. Sources are given in Table S5.

regime that may be caused by increased parasitic absorption within the stack. We speculate that the light scattering properties of the nanotextures adversely increase the near-infrared (NIR) absorption of PEDOT:PSS (Figure S18), as has been found before for different photovoltaic systems [17, 42–44]. To overcome these limitations, we explored a SAM/graphene oxide (GO) bilayer with negligible absorption losses as an alternative HTL combination (schematic layer stack in Figure 3d). We studied the associated changes for the NBG subcell in our recent publication [45]. The bilayer-based APTSC shows strongly reduced parasitic absorption losses in the NIR, delivering an increased integrated current density of 16.78 mA•cm^{-2} in the NBG cell, while the top cell reaches 17.33 mA•cm^{-2}. A summary of the (equivalent) current densities achieved in the optical optimization process of APTSCs is displayed in Figure S19.

This high photogeneration in the bilayer-based tandem on nanotexture is also translated to a high J_{SC} in JV curves, reaching 17.18 mA cm^{-2} (Figure 3e). This value lies between the integrated J_{SC} values for top and bottom subcells from the EQE measurements

16163028, 2026, 76, Downloaded from https://advanced.onlinelibrary.wiley.com/doi/10.1002/adfm.77815 by Helmholtz-Zentrum Berlin Für, Wiley Online Library on [10/11/2026]. See the Terms and Conditions (https://onlinelibrary.wiley.com/terms-and-conditions) on Wiley Online Library for rules of use; OA articles are governed by the applicable Creative Commons License

(Figure 3d) and could originate from a low shunt resistance in the bottom subcell (cf. Note S3 and Table S4 and Figure S20) [46]. Further improvements in current matching conditions could be achieved by increasing the bandgap of the top cell, thereby increasing the Br content and potentially defect densities as well [47]. A more luminescent top cell could also help relax the current matching conditions and would benefit from the reduced parasitic absorption of the bilayer [48]. Another option is the fabrication of a thicker bottom subcell absorber, which has shown great effect before [8], although this demands long carrier diffusion lengths in the Sn-Pb perovskite to ensure efficient charge extraction [49]. Compared to recent literature reports – with a tandem Voc >1.9 V and a Sn-Pb perovskite in the bottom subcell – our achieved tandem J_{SC} ranks among the highest values for APTSCs (Figure 3f), surpassing 90% of the theoretical limit of photocurrent density. From the JV measurements, the bilayer-based tandem on nanotextures delivers a PCE of 27.98% (reverse scan) with a stabilized power output of 27.5% after 600 s of maximum power point (MPP) tracking (Figure 3e), presenting a significant improvement over the planar tandem cell (24.8% PCE after 600 s of MPP tracking) with PEDOT:PSS and a thin front TCO. Under long-term MPP tracking at 25°C in N_2, unencapsulated planar and nanotextured APTSCs employing PEDOT:PSS show a decrease in PCE to 80% of the initial value (T_{80} lifetime) after 175 h and 115 h, respectively (Figure S21).

2.3 | Optical Potential of APTSCs Guided by Optical Simulations

The experimentally optimized APTSCs show that front-sided nanotexturing greatly reduces the overall reflection losses of APTSCs, consequently increasing the matched tandem J_{SC} and confirming our previous theoretical study [17]. In this final section, we aim to give an outlook and explore the optical potential of APTSCs with optical simulations. We take several assumptions beyond state-of-the-art APTSCs, including micrometer-sized textures, based on technological advancements in other perovskite-based research fields. For this, the simulation package GenPro4 [24] for MatLab is used. Representing a solar cell as a multilayer structure, it combines wave and ray optics, taking interference and light scattering into account, and enables time-efficient screening of device configurations (simulation details provided in the method section, and complex refractive index (*nk)* datasets are summarized in Table S6).

To validate our optical model, we first compared a simulation of a planar APTSC with the respective experimentally measured EQE and reflectance (Figure S22). Both WBG and NBG absorption onsets and the overall shape of simulated absorption and measured EQE spectra fit well, indicating that layer thickness and *nk*-datasets are appropriate. In the following, all simulations include an anti-reflective coating of NaF for an air/glass interface.

Similar to our experimental optimization, we simplified the interconnect of APTSCs in a planar superstrate configuration. Figure 4a shows that subsequently removing PEDOT:PSS as HTL and IZO as recombination layer increases absorption in the NBG, similar to the experimental findings in Figure 3. Such a simplified interconnect has also been reported experimentally before [50–52] and strongly relies on a robust ALD SnO_x layer to protect the underlying perovskite subcell. In addition to the inherently high reflection losses due to thin film interferences, we observe a local reflectance maximum at 700 nm (dashed lines in Figure 4a). This is in agreement with our experimental results, where this phenomenon is observed for both planar (Figure 3b) and nanotextured APTSC (Figure 3c,d). When comparing the refractive indices of the WBG, C_{60}, SnO_x and NBG between 600 and 1100 nm (Figure S23), it becomes evident that the refractive index (n) mismatch between the layers leads to reflection losses. Such mismatch between subcells has been addressed by tuning the refractive index of nc-SiOx in PSiTSCs [21]. In our case, we numerically explored the effect by increasing n of the SnO_x layer. Figure 4b,c show the effect on planar APTSCs with 20 and 80 nm SnO_x intermediate layers, respectively. The change in refractive index lowers the reflection in the 700–900 nm range: this effect is stronger for an 80 nm thick SnO_x layer (Figure 4c). Shifting the refractive index of SnO_x between the WBG (2.34 @700 nm, Figure S23) and NBG (2.53 @700 nm, Figure S23) visibly reduces the reflection, as expected by the ideal refractive index for minimum reflection at $n_{ideal} = 2.43 = \sqrt{2.34 \cdot 2.53}$ ($\lambda = 700\ nm$) [53]. We note that while the shift of refractive index by a constant value is not consistent with the Kramers-Kronig relationship, the considered values could be realized by several strategies, e.g., adjusting the deposition temperature during ALD growth [54, 55], controlling the nucleation [56, 57], or utilizing high-refractive index metal oxides such as TiO_2 [58, 59]. We assume that the implementation of these examples is feasible for APTSCs while maintaining good electrical properties of the buffer layers. Depending on the implemented SnO_x layer thickness, which is dictated by fabrication constraints, a photocurrent gain of 0.14–0.67 mA•cm^{-2} can be expected for 20 and 80 nm, respectively.

As we have shown above, implementing nanotextures into APTSCs improves light in-coupling and reduces reflection losses. In the following, we move beyond the nanotextures and numerically investigate the incorporation of random pyramids into the superstrate APTSCs stack that we used in Figure 4a, based on our reference SnO_x *nk*-set [60] again. While the scattering mechanism may differ from the nanotextures, random pyramids approach the Yablonovitch limit of light trapping, enhancing the absorption by a factor of up to $4n^2$ in the low-absorbing regime [61] and serve here as an estimate for an upper limit of light absorption. These micron-sized pyramids have been demonstrated for PSiTSCs before [62] and are well integrated into GenPro4. A height map of the texture used for simulations is given in Figure S24.

For an APTSCs stack in superstrate configuration, we first considered a front + middle (*fr. + mid.*) textured stack (faded line) and a *fully textured* stack (saturated line) in Figure 4d, essentially differing only at the back contact. Both variations are based on a planar air/glass interface. The *fr. + mid* texture reduces reflection losses of the tandem stack, especially in the NBG regime. Additionally, the NBG response close to its band edge is well enhanced, with a steeper rise compared to the planar case.

Importantly, the middle texture improves the in-coupling of light from the WBG into the NBG subcell, as evident from the absence of a step in the reflectance spectrum at 700 nm (dashed line, Figure 4d). These trends are similar to the trends observed in [17], where sinusoidal nanotextures were considered. Finally, the

16163028, 2026, 76, Downloaded from https://advanced.onlinelibrary.wiley.com/doi/10.1002/adfm.77815 by Helmholtz-Zentrum Berlin Für, Wiley Online Library on [10/11/2026]. See the Terms and Conditions (https://onlinelibrary.wiley.com/terms-and-conditions) on Wiley Online Library for rules of use; OA articles are governed by the applicable Creative Commons License

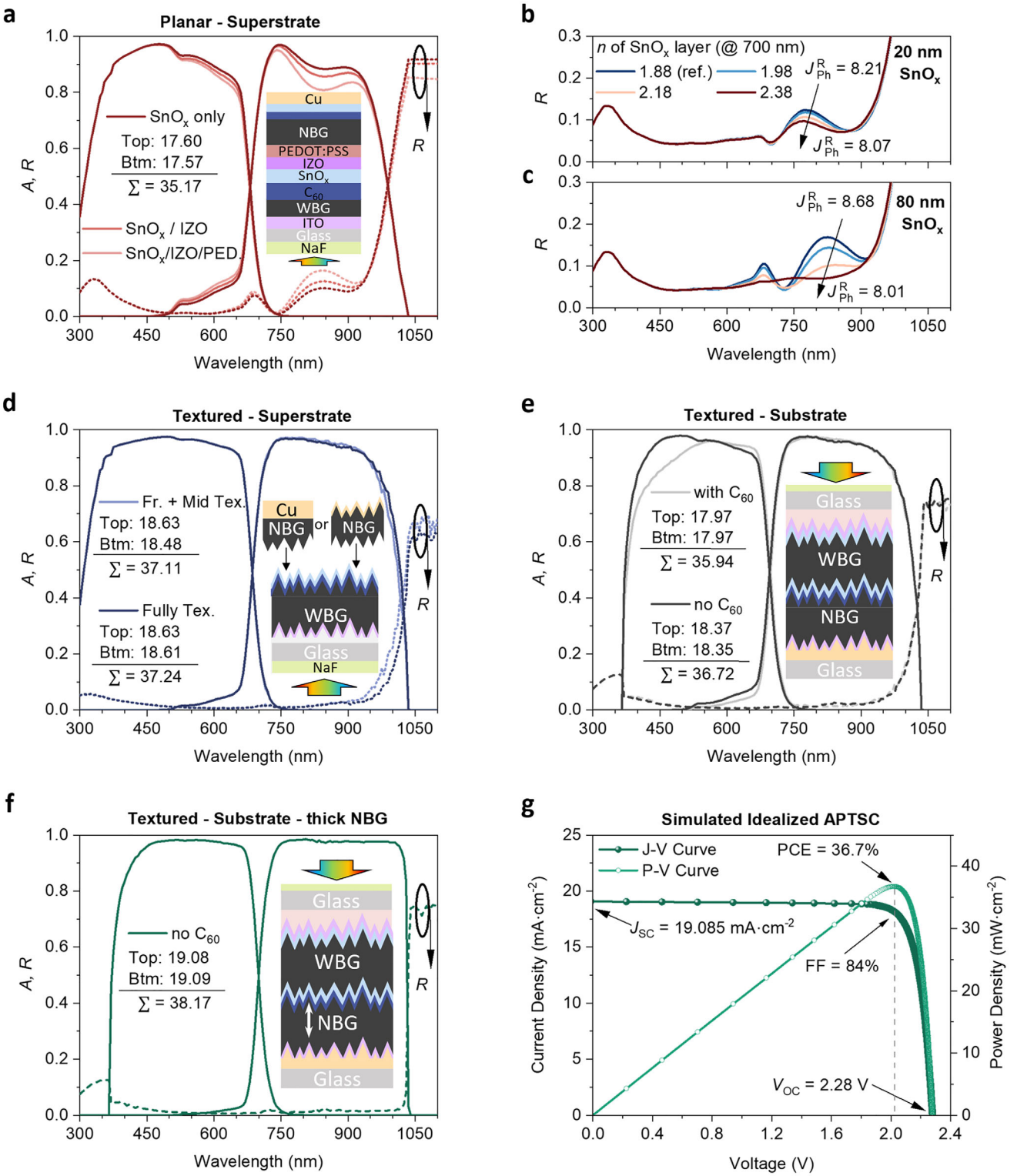


FIGURE 4 | Optically simulated absorptance and reflectance spectra of APTSCs. (a) Simulation of a fully planar stack in superstrate configuration, with simplified interconnecting layer by (1) removing PEDOT:PSS and (2) the sputter-deposited IZO layer. (b,c) Index matching of the interconnecting SnO_x layer (20 nm and 80 nm, respectively) by adding a constant offset to its refractive index. (d) Simulation of an APTSC in superstrate configuration with the incorporation of random pyramid textures, either with a flat or textured back contact. (d) Simulation of pyramidally textured APTSCs in substrate configuration with glass/EVA considered at the top. (f) Fully textured APTSCs in substrate configuration where the use of a 20 μm thick NBG absorber (e.g., grown as single crystal) is considered. (g) Simulated J-V curve of an idealized APTSCs in the upper limit scenario of light absorption from (e); V_{oc} and FF are based on the discussion in [77]. The inset figures show the APTSC layer stack. It must be noted that for improved clarity, not all functional layers of the APTSC are labelled. All implied current density values are given in mA•cm^{-2}.

16163028, 2026, 76, Downloaded from https://advanced.onlinelibrary.wiley.com/doi/10.1002/adfm.77815 by Helmholtz-Zentrum Berlin Für, Wiley Online Library on [10/11/2026]. See the Terms and Conditions (https://onlinelibrary.wiley.com/terms-and-conditions) on Wiley Online Library for rules of use; OA articles are governed by the applicable Creative Commons License

absorption in the NBG subcell is increased from 17.57 mA•cm^{-2} (*planar*) to 18.48 mA•cm^{-2} (*fr. + mid. texture*). These simulations present idealized scenarios indicating an upper limit for the photocurrent density. However, conformal coating of perovskite (top) cells was reported for co-evaporation [63] and 2-step hybrid methods [64] in PSiTSCs, solution-based on ordered nano- or microstructures [65] and sequential thermal evaporation for Sn-Pb perovskites [66, 67]. To realize *fr. + mid. textured* APTSCs, the NBG absorber thickness would need to be larger than the texture size to planarize the back contact. If the NBG is coated conformally as well, a *fully textured* APTSC could be realized. Interestingly, the simulation results of a *fully textured* stack (Figure 4d) only show a slight enhancement along the absorption onset of the NBG to 18.61 mA•cm^{-2}, due to the textured back contact. The gain for the *fully textured* APTSC is limited by the increased parasitic absorption in the Cu electrode from 1.10 to 1.53 mA•cm^{-2} (Figure S25) as reported previously [17] and could be addressed by inserting a buffer layer between the absorber and the electrode [18, 22, 68].

So far, we only considered APTSCs in superstrate configuration, where light enters through the carrier glass used for deposition and which is the experimentally prevalent configuration for APTSCs. Next, we simulate APTSCs in substrate configuration, where light enters through the layer deposited last. This underreported architecture for APTSCs may enable improved device stability [69] and open up new processing and light trapping options. Figure 4e depicts the absorption and reflectance spectra of a fully textured APTSCs stack in substrate configuration. Here we considered a glass sheet at the top bonded with a 200 µm thick ethylene vinyl acetate (EVA) layer to the APTSC stack [70]. Compared to the superstrate configuration, the reflectance losses increase from 3.60 mA•cm^{-2} (superstrate) to 3.92 mA•cm^{-2} (substrate), due to the different front-facing layers. The absorption of the NBG subcell is similar to the superstrate configuration, while the WBG shows a clear change for the two considered variations – *with* (faded line) and *without* C_{60} (saturated line) on top of the WBG. With C_{60} in place, the top cell suffers from parasitic absorption in the C_{60} layer (Figure S26), limiting its implied photocurrent density to 17.97 mA•cm^{-2}. When removing the C_{60} layer, the top cell absorption can be enhanced to 18.37 mA•cm^{-2} while maintaining current matching conditions. These results fall short compared to the superstrate configuration, which for the *fully textured* case reaches 18.94 and 18.98 mA•cm^{-2} in the top and bottom subcell, respectively. The fully textured substrate configuration therefore relies on ETL materials which show low parasitic losses, e.g., non-fullerene ETLs [71, 72], as well as suitable encapsulation materials.

Going a step further, we explored the upper limit of light absorption in the NBG subcell by considering the use of 20 um thick NBG absorbers. Efficient perovskite solar cells with such layer thickness were reported for single-crystal-like Pb-based perovskite films with long carrier diffusion lengths, e.g in $MAPbI_3$ [73], mixed MA-FA [74], and with mixed halides [75], while single-crystal Sn-Pb perovskites have been reported as photodetectors [76]. With the assumption of combining these advancements, this scenario acts as an estimate for an upper limit of light absorption, with single-crystal Sn-Pb perovskites as a prerequisite. Building upon the fully textured substrate configuration without C_{60}, Figure 4f shows the simulation results of a 20 µm thick NBG layer. The bottom subcell absorption above 900 nm is greatly enhanced, with an extremely sharp onset and an almost rectangular shape. Consequently, the implied photocurrent densities reach 19.08 and 19.09 mA•cm^{-2} for the top and bottom subcell, respectively. An overview of implied J_{ph} values for the optical simulations is given in Figure S27.

In summary, our simulations suggest that a simplified interconnect will improve the bottom cell absorption, while index matching or textured interfaces will reduce reflectance losses. A fully textured stack is beneficial for both the superstrate and substrate configuration, where the latter benefits more due to a textured interface toward air. Strategies to inhibit parasitic absorption in the back contact should be implemented. In the idealized case, exploiting the fundamental Yablonovitch light trapping limit with a fully textured APTSCs in substrate configuration, having a lossless ETL and a thick NBG, a combined J_{ph} of 38.17 mA•cm^{-2} could be reached. Assuming that this J_{Ph} can be equally divided between the subcells and that they reach 94% of their respective detailed balance limit in V_{OC} (1.39 V for top subcell and 0.89 V for bottom subcell) [77] and in analogy also in FF (86% for top subcell and 83% for bottom subcell), we modelled the resulting subcell and tandem J-V curves based on a diode model. The resulting tandem solar cell J-V curve shows a J_{SC} of 19.085 mA cm^{-2}, a V_{OC} of 2.28 V, and a FF of 84%, which would imply a potential PCE of 36.7% (Figure 4g).

3 | Conclusion

In this work, we evaluated optical design strategies in experiment and simulation, enabling a systematic advancement in the optical design of monolithic all-perovskite tandem solar cells (APTSCs). We experimentally investigated the effects of front-sided nanotextures and contact layer optimizations for the optics of APTSCs. An investigation of the WBG perovskite top cell's film properties on nanotextures revealed enhancements in V_{OC} and J_{SC} over planar substrates. For APTSCs, the front-side nanotextures improved light in-coupling over the whole absorption range and minimized thin-film interference effects to consequently boost light absorption in both subcells. In conjunction with a tailored front ITO and GO/SAM bilayer for the NBG, we reduced parasitic absorption in the NIR and systematically improved the APTSC J_{SC} toward 17.18 mA cm^{-2} with a PCE of 27.98% (MPP: 27.5%). Optical simulations delivered a perspective for future optical gains in APTSCs: high *n* interconnecting layers can reduce Fresnel reflection at planar interfaces. Furthermore, the implementation of fully textured interfaces can suppress such reflections even more strongly and increase the band edge absorption in the perovskite absorbers. Simulations of a fully textured APTSCs in substrate configuration show that a front-sided ETL with low parasitic absorption is crucial to unlock similar optical performance as the superstrate counterpart. However, exploiting thick single-crystal-like Sn-Pb perovskites in a fully textured substrate configuration would increase the photocurrent and enable PCEs exceeding 35 %. This work is a guideline to further enhance the optics of monolithic APTSCs and potentially other all-perovskite multijunction solar cells with more than two absorbers.

16163028, 2026, 76, Downloaded from https://advanced.onlinelibrary.wiley.com/doi/10.1002/adfm.77815 by Helmholtz-Zentrum Berlin Für, Wiley Online Library on [10/11/2026]. See the Terms and Conditions (https://onlinelibrary.wiley.com/terms-and-conditions) on Wiley Online Library for rules of use; OA articles are governed by the applicable Creative Commons License

4 | Methods Section

4.1 | Materials

CsI (99.999%) was purchased from abcr. FAI and MACl were purchased from GreatCell Solar Materials. PbI_2 (99.99%, trace metals basis), $PbBr_2$ (>98.0%), and $PbCl_2$ (sublimed, >99.5%) were purchased from Tokyo Chemical Industry Co., Ltd. (TCI).

(4-(3,6-Diphenyl-9H-carbazol-9-yl)butyl)phosphonic acid (Ph4PACz) (>99%) was purchased from Luminescence Technology Corp. Anhydrous dimethylformamide (DMF, 99.8%), dimethylsulfoxide (DMSO, >99.99%), iso-propanol (IPA, 99.5%), and Ethane-1,2-diammonium iodide ($EDAI_2$, >98%) were purchased from Sigma-Aldrich. Ethanol (EtOH, anhydrous) was purchased from VWR. Fullerene C_{60} (sublimed, >99.99%) was purchased from CreaPhys GmbH. Tetrakis(dimethylamino)tin(IV) (TDMASn, precursor for atomic layer deposited SnO_x) was purchased from STREM Chemicals, Inc. Cu pellets were purchased from Alfa Aesar. 0.2 µm PTFE filters were purchased from Whatman. Glass substrates (25 × 25 mm, 0.7 mm thickness) and anti-reflective foil (AFH 3090) were purchased from Yingkou Libo New Energy Technology Co., Ltd.

2-Aminoethanaminium iodide (AEAI) was synthesized as reported in the literature [78]. Briefly: ethylenediamine (1 mL, 15 mmol; 99.9%, Sigma–Aldrich) was dissolved in 10 mL of anhydrous ethanol in an ice bath. Then, hydriodic acid (14.25 mmol, 0.95 eq, 57 wt. water, 99.95% Acros) was added while stirring. The white precipitate has been rapidly filtered and washed with abundant dry ethanol and placed under vacuum to dry overnight at room temperature. 1H NMR (300 MHz, DMSO-d6) δ 8.40 – 8.12 (bs, 5H), 3.18 (s, 4H).

4.2 | Preparation of WBG Perovskite Precursor Solution

To obtain a 1 M perovskite solution with the nominal composition of $FA_{0.78}Cs_{0.22}Pb(I_{0.7}Br_{0.3})$, CsI (57.16 mg), FAI (134.14 mg), $PbBr_2$ (165.15 mg), and PbI_2 (253.56 mg) were mixed in *vial 1* with 1 mL DMF:DMSO (3:1 v:v). The solution was stirred for up to 16 h at 25°C. In *vial 2*, 1 M of the nominal composition $MAPbCl_3$ was scaled with MACl (6.75 mg) and $PbCl_2$ (27.81 mg). To yield the final solution, all of the solution from *vial 1* is transferred into *vial 2* and stirred at 25°C for 2 h. A vortexer is used to aid with dissolving. Finally, the solution is filtered through 0.2 µm PTFE filters into *vial 3*. For the solar cell fabrication, precursor solutions with a concentration between 1.2 and 1.4 M before filtering were used.

4.3 | Preparation of NBG Perovskite Precursor Solution

A total of 2 M perovskite precursor solution with the nominal composition of $(CsI)_{0.07}((FA_{0.7}MA_{0.3})(Pb_{0.45}Sn_{0.55})I_3)_{0.93}$ was prepared by mixing SnF_2 (34.8 mg), CsI (72.8 mg), MAI (190.8 mg), FAI (481.6 mg), PbI_2 (829.8 mg), SnI_2 (819.5 mg), Sn(0) (13.1 mg) in one vial with 2 mL of DMF:DMSO (3:1 v:v) and shaken overnight, resulting in more than 2.2 mL perovskite solution. 30 min before spin-coating, 2.2 mL of perovskite precursor solution was added to 5 mg of GlyHCl in a second vial and stirred until fully dissolved. Afterward, the solution was filtered through a 0.2 µm PTFE filter.

4.4 | WBG Single Junction Fabrication

Planar and nanotextured substrates are cleaned in a sequence in Mucasol, DI water, and isopropyl alcohol within an ultrasonic bath for 15 min each. Between each step, the substrates are washed several times with DI water. Afterward, the cleaned substrates are blown dry with a N_2 gun and put into a UV-O_3 cleaner (UVOH 150Lab from FHR) for 20 min. Then, they are immediately transferred to a glovebox. A SAM is deposited atop the treated substrates by spin-coating 100 uL of Ph4PACz (0.5 mg mL^{-1} in ethanol) for 20 s at 3000 r.p.m, including a ramp-up of 5 s. The films are annealed for 10 min at 100°C in the glovebox. The WBG perovskite film is then deposited by spin-coating by dropping 100 uL of precursor solution atop the SAM and spreading it with a clean and fresh pipette tip. The substrate is spun at 5000 r.p.m. for 40 s, including a 5 s ramp-up. 200 uL of methyl acetate is dropped quickly and close to the surface at 15 s before the end of the process. The film is annealed at 100°C for 20 min in the glovebox. Afterward, the perovskite surface is passivated by dynamically spin-coating 100 uL of AEAI (1 mg mL^{-1} in IPA) at 5000 r.p.m. for 20 s, including a 2.5 s ramp-up, followed by annealing the film at 100°C for 5 min. Then 18 nm of C_{60} via thermal evaporation and 35 nm of SnO_2 by atomic layer deposition are deposited atop. In the end, 100 nm of Cu is thermally evaporated to complete the solar cell.

4.5 | All-Perovskite Tandem Solar Cell Fabrication

The fabrication of APTSCs follows the WBG single junctions until after the ALD SnO_x layer. Then, a 40 nm IZO layer is sputter-deposited atop through a shadow mask to separate the layer for each pixel. The samples are loaded through air into a load-lock, which is evacuated and then transferred in vacuum to the sputtering chamber. An Ar/O_2 gas mixture is used for the sputtering process.

Afterward, PEDOT:PSS (Heraeus Al 4083 1:1 with IPA v:v, sonicated for 10 min at RT and filtered through a PTFE filter) is spin-coated atop the recombination layer, at 6000 r.p.m. for 30 s including 2.5 s ramp-up. The wet films are intermediately stored in a vacuum chamber for 5 min at −1 mbar and then transferred into a glovebox and annealed at 100°C for 10 min.

For the bilayer-based tandem solar cells, Graphene Oxide (GO) dispersion from GOO is diluted with DI water to a concentration of 1 mg mL^{-1} and sonicated for at least 30 min. The solution is used without filtering. GO layer is spin-coated in ambient air at 4000 r.p.m. for 30s with an acceleration of 1000 r.p.m.•s^{-1}. The samples are annealed for 10 min at 100°C in ambient air and afterward transferred to a glovebox.

Then the NBG perovskite is spin-coated by dropping 100 uL of precursor solution onto the sample and spun first at 1000 r.p.m. for 15 s, including a 5 s ramp-up, then at 4000 r.p.m. for 40 s, including a 5 s ramp-up. 250 uL toluene is dropped onto the

16163028, 2026, 76, Downloaded from https://advanced.onlinelibrary.wiley.com/doi/10.1002/adfm.77815 by Helmholtz-Zentrum Berlin Für, Wiley Online Library on [10/11/2026]. See the Terms and Conditions (https://onlinelibrary.wiley.com/terms-and-conditions) on Wiley Online Library for rules of use; OA articles are governed by the applicable Creative Commons License

spinning film at 10 s before the end of the program. The NBG film is annealed at 100°C for 10 min. Directly afterward, the surface treatment is applied by dynamically spin-coating $EDAI_2$ solution (0.75 mg in IPA, filtered through a PTFE filter) at 3000 r.p.m. for 30 s, including a 2 s ramp-up time. The films are then annealed at 100°C for 5 min. Finally, 23 nm C_{60} is thermally evaporated on top, followed by 20 nm ALD SnO_2 and 100 nm Cu by thermal evaporation.

4.6 | Fabrication of Nanotextures

The sinusoidal nanotextures were prepared on cleaned silicate glasses from Yingkou Libo New Energy Technology CO., Ltd. The procedure follows our earlier report [23].

4.7 | Sputter-Deposition of Front ITO

Indium tin oxide films were deposited using an in-line pulsed DC magnetron sputtering system from Leybold Optics (A600V7). The ITO layers were deposited from a planar target (600 mm, EVOCHEM GmbH) at a substrate temperature of approximately 330°C and at varying oxygen flow ratios relative to argon (Ar) of 1.2%, 2.0%, and 3.2%. The radiative heaters were set to 621°C and 471°C. Prior to deposition, the sputter chamber was maintained overnight at the heater temperature settings. The base pressure before deposition was approximately 2×10^{-6} mbar. The process pressure was 5.7×10^{-3} mbar at a total gas flow of 570 sccm. The sputter power was set to 4 kW, and pulsing was performed at a frequency of 40 kHz with a pulse duration of 1.2 µs.

4.8 | Solar Cell Device Characterization

The current density–voltage (*J–V*) characteristics of the solar cells were measured using a digital source meter (Keithley Model 2400) under simulated 1 Sun AM 1.5G illumination (1000 W m^{-2}), provided by a Wavelabs Sinus 300 LED solar simulator at 25°C in a nitrogen (N_2) atmosphere. The light intensity and spectrum were calibrated prior to measurement using a silicon reference cell (KG3 filtered or unfiltered). *J–V* measurements were performed by first scanning in the reverse direction (from forward bias to short circuit), followed by a forward scan (from short circuit to forward bias), with voltage steps of 20–40 mV. For each point, the integration time and settling time were both set to 20 ms. The device active area was defined using a metal mask with an aperture area of 0.1 cm^2 (single-junction) or 0.1225 cm^2 (Tandem). Short-term maximum power point (MPP) tracking for stabilized power output was conducted using the same setup, with a step size of 10 mV, a tracking time of 1 s per step, and an integration time of 20 ms.

4.9 | External Quantum Efficiency

External quantum efficiency (EQE) measurements were carried out in ambient air using a QE-R system (EnliTech). For Sn–Pb perovskite and tandem devices, encapsulation was performed with a glass coverslip and bluefix resin, cured under a UV lamp, prior to measurement in air. The EQE system was calibrated before each measurement using a silicon reference detector. The modulation frequency was 210 Hz. For tandem device measurements, the sample was illuminated with external light bias from ThorLabs LIU series LED arrays positioned close to the device. For top subcell measurements, an LED with a center wavelength of 850 nm was used, and for bottom subcells, an LED with a center wavelength of 470 nm was used, respectively.

4.10 | Photoluminescence

Steady-state PL measurement was performed by using a home-built setup with a 520 nm laser. The power density of the laser was approximately one sun intensity, with a spot size approximately 1.5 mm in diameter. The quasi-Fermi level splitting (QFLS) is calculated with the following equation. $QFLS = k_B{*}T{*}\ln(PLQY{*}J_G/J_0)$, where k_B is the Boltzmann constant, PLQY is photoluminescence quantum yield, T is the temperature, J_G is the generation current density, and J_0 is the dark recombination current density.

4.11 | Transient Surface Photovoltage

trSPV measurements were carried out on an in-house-built setup. The samples were laser-excited with a tunable pumped pulse laser (Nd:YAG Laser, EKSPLA, NT230-50-SH/SF-SCU-2H) that was guided through a beam expander and a diaphragm with an opening of ~7 mm, before passing through a quartz cylinder with a diameter of 7 mm right onto the sample surface. For the measurements in this work, an excitation energy of 2 eV and a pulse time of 3–6 ns at a measurement frequency of 2 Hz were used. The laser fluence was controlled via neutral density filters and adjusted to yield charge carrier densities equivalent to 1 Sun. The transients were measured with an oscilloscope card (Gage, CSE 1622- 4GS, 200 MS s−1) using in-house developed software for logarithmic read-out. We illuminated and measured the SPV of all samples from the perovskite side to exclude optical effects by the nanotextured substrate.

4.12 | Atomic Force Microscopy

Atomic force microscopy (AFM) measurements were performed with an XE-70 AFM by Park Systems, featuring a nanoscopic high aspect ratio tip.

4.13 | X-Ray Diffraction

XRD diffractograms were obtained with a Bruker D8 diffractometer in Bragg-Brentano geometry. The perovskite films were measured in ambient air at room temperature. No encapsulation was used. For all measurements, the Cu K-alpha radiation emitted from an X-ray tube operated at 40 mA and 40 kV acceleration voltage was used with a step size of 0.02 2Theta and 1 s integration time.

16163028, 2026, 76, Downloaded from https://advanced.onlinelibrary.wiley.com/doi/10.1002/adfm.77815 by Helmholtz-Zentrum Berlin Für, Wiley Online Library on [10/11/2026]. See the Terms and Conditions (https://onlinelibrary.wiley.com/terms-and-conditions) on Wiley Online Library for rules of use; OA articles are governed by the applicable Creative Commons License

4.14 | Scanning Electron Microscopy

SEM measurement was conducted using a MERLIN FE-SEM with a GEMINI II optical column from Zeiss. The acceleration voltage was 3 kV at a current of 50 pA. An InLens detector was used for the images.

4.15 | UV–Vis Spectroscopy

The reflection and transmission of films and solar cells were measured with a PerkinElmer Lambda-1050 UV–vis–NIR spectrometer with 5 nm steps from 1100 to 300 nm. A white standard (Spectralon) was used for calibration before characterization.

4.16 | Optical Simulations

Optical simulations were performed with the GenPro4 software from TU Delft ([24]). The *nk* data used herein are summarized in Table S6, except for the front ITO. The front ITO *nk* data set was obtained by spectral ellipsometry of thin films on polished Si wafers. A Drude-Lorentz model was applied to model a spectral range from 190 to 2400 nm. The simulation stacks generally consisted of 4 media with varying coatings: air/glass/NBG/Ag, i.e., the NBG was modeled incoherently for thicknesses between 1 and 20 μm. The detailed layer stacks for the various architectures are depicted in the respective figures. TCO, C60, SnO2, and NaF layers were modelled as coatings at the respective interfaces. We omitted the modelling of the self-assembled monolayers in all simulations. The given implied current density values are calculated based on the AM1.5G reference spectrum. Current matching was achieved by varying the top cell thickness in increments of 25 nm in all cases. For the simulation of substrate configurations, a 1.78 eV top cell was simulated by offsetting the 1.8 eV *nk*-set by 7 nm toward lower wavelengths.

4.17 | Electrical Simulations With Quokka3

Quokka3 [25] was used to evaluate series resistance (R_S) losses when changing the TCO thickness. An ITO resistivity of 187 μΩ cm was measured and assumed to be constant throughout the thickness variation. The calculated power loss associated with a change in R_S was then combined with optical losses and is described in Note S1.

Author Contributions

S.B. fabricated all WBG films, conducted JV, EQE, UV–vis, XRD measurements and analysis, optical simulations, and wrote the first draft of the manuscript. P.T and S.A conceived the idea and supervised the work. Y. Y., D.I., I. T. and V.V. fabricated NBG films to complete the tandem devices. A. C. and M. H. developed and optimized the front ITO sputtering process. B. L and K. J. P. optimized the recombination IZO sputtering process. D. M., Sh. M. and Si. M. conceived and synthesized the passivation molecule. H. W. conducted AFM measurements and analysis. T. G. conducted trSPV measurements and analysis. F. R. fabricated the nanotextures on glass. K. J. assisted with the optical simulations. K. J. and C. B. supported the analysis of optical solar cell performance. R. A. J. J., S. L., B. S., C. B., and S. A. provided the funding. All authors assisted in improving the manuscript.

Acknowledgements

The authors thank J. Beckedahl, M. Choyne, C. Ferber, M. Wittig, T. Lußky, and H. Heinz for the technical support in the HySPRINT Helmholtz Innovation Lab. The authors thank T. Dittrich for the technical assistance and support during data evaluation for trSPV measurements, as well as Katja Mayer-Stillrich and Manuel Hartig for sputtering deposition. The authors thank the German Federal Ministry of Research, Technology and Space (BMFTR) for funding the projects "PEROWIN" (03SF0631) and "TeamPV" (03SF0747). Further funding was provided by the Helmholtz Association via projects "Zeitenwende – Beschleunigter Transfer der nächsten Generation von Solarzellen in die Massenfertigung" and the HySPRINT Helmholtz Innovation Lab. In addition, we acknowledge the research school "HyPerCells". The authors further thank the Deutsche Forschungsgemeinschaft (DFG) for funding through the project "HIPSTER PRO" (grant no. AL 2241/1-1), the EUROPEAN CLIMATE, INFRASTRUCTURE AND ENVIRONMENT EXECUTIVE AGENCY (CINEA), Project 101075605 – SuPerTandem, the European Union's Horizon Europe research and innovation programme under grant agreement No. 101162377 (Jump into Space) and the European Research Council under agreement No. 101098168 (PERSTACK). S. A. acknowledges funding by the Alexander von Humboldt Foundation through a Feodor-Lynen Research Fellowship.

Open access funding enabled and organized by Projekt DEAL.

Funding

This work was supported by the "PEROWIN" (03SF0631), "TeamPV" (03SF0747), "HIPSTER PRO" (grant no. AL 2241/1-1), "SuPerTandem" (101075605), "Jump into Space" (101162377), and "PERSTACK" (101098168).

Conflicts of Interest

The authors declare no conflicts of interest.

Data Availability Statement

The data that support the findings of this study are available from the corresponding author upon reasonable request.

References

1. T. Moot, J. Werner, G. E. Eperon, et al., "Choose Your Own Adventure: Fabrication of Monolithic All-Perovskite Tandem Photovoltaics," *Advanced Materials* 32 (2020): 2003312.

2. R. Tian, K. Sun, Y. Meng, et al., "Chemical Hardness Engineering Synchronizes Crystallization In Perovskite Tandems," *Nature Nanotechnology* 21 (2026): 810–820.

3. C. Liu, Y. Yang, H. Chen, et al., "Bimolecularly Passivated Interface Enables Efficient And Stable Inverted Perovskite Solar Cells," *Science* 382 (2023): 810–815.

4. F. Yang, P. Tockhorn, A. Musiienko, et al., "Minimizing Interfacial Recombination in 1.8 eV Triple-Halide Perovskites for 27.5% Efficient All-Perovskite Tandems," *Advanced Materials* 36 (2024): 2307743.

5. Z. Liu, R. Lin, M. Wei, et al., "All-Perovskite Tandem Solar Cells Achieving> 29% Efficiency With Improved (100) Orientation In Wide-Bandgap Perovskites," *Nature Materials* 24 (2025): 252–259.

6. R. Lin, K. Xiao, Z. Qin, et al., "Monolithic All-Perovskite Tandem Solar Cells With 24.8% Efficiency Exploiting Comproportionation To Suppress Sn(ii) Oxidation In Precursor Ink," *Nature Energy* 4 (2019): 864–873.

7. S. Hu, J. Wang, P. Zhao, et al., "Steering Perovskite Precursor Solutions For Multijunction Photovoltaics," *Nature* 639 (2024): 93–1010.

16163028, 2026, 76, Downloaded from https://advanced.onlinelibrary.wiley.com/doi/10.1002/adfm.77815 by Helmholtz-Zentrum Berlin Für, Wiley Online Library on [10/11/2026]. See the Terms and Conditions (https://onlinelibrary.wiley.com/terms-and-conditions) on Wiley Online Library for rules of use; OA articles are governed by the applicable Creative Commons License

8. R. Lin, J. Xu, M. Wei, et al., "All-Perovskite Tandem Solar Cells With Improved Grain Surface Passivation," *Nature* 603 (2022): 73–78.

9. Z. Zhang, R. Zhu, Y. Tang, et al., "Anchoring Charge Selective Self-Assembled Monolayers for Tin–Lead Perovskite Solar Cells," *Advanced Materials* 36 (2024): 2312264.

10. C. Liu, R. Lin, Y. Wang, et al., "Efficient All-Perovskite Tandem Solar Cells with Low-Optical-Loss Carbazolyl Interconnecting Layers," *Angewandte Chemie International Edition* 62 (2023): 202313374.

11. K. Datta, J. Wang, D. Zhang, et al., "Monolithic All-Perovskite Tandem Solar Cells with Minimized Optical and Energetic Losses," *Advanced Materials* 34 (2022): 2110053.

12. Z. Yu, J. Wang, B. Chen, et al., "Solution-Processed Ternary Tin (II) Alloy as Hole-Transport Layer of Sn–Pb Perovskite Solar Cells for Enhanced Efficiency and Stability," *Advanced Materials* 34 (2022): 2205769.

13. S. Fu, N. Sun, Y. Xian, et al., "Suppressed Deprotonation Enables A Durable Buried Interface In Tin-Lead Perovskite For All-Perovskite Tandem Solar Cells," *Joule* 8 (2024): 2220–2237, https://doi.org/10.1016/j.joule.2024.05.007.

14. K. H. Seo, S. Biswas, Y. Lee, et al., "Uncovering the Underlying Electromagnetic Mechanism Of Lead-Free All-Perovskite Tandem Solar Cells With ZnO Moth-Eye Antireflection Layers," *Dyes and Pigments* 235 (2025): 112619.

15. Y. Ge, L. Zheng, H. Wang, et al., "Suppressing Wide-Angle Light Loss And Non-Radiative Recombination For Efficient Perovskite Solar Cells," *Nature Photonics* 19, no. 2 (2025): 170–177.

16. C. Liu, H. Gao, W. Ou, H. Tan, and R. Lin, "Light Management In Monolithic All-Perovskite Tandem Solar Cells," *Light: Science & Applications* 15 (2026): 56.

17. K. Jäger, A. Tejada, S. Berwig, et al., "Optical Simulations of Nanotextured All-Perovskite Tandem Solar Cells," *Advanced Theory and Simulations* 8 (2025): 2400724.

18. P. Tockhorn, J. Sutter, A. Cruz, et al., "Nano-Optical Designs For High-Efficiency Monolithic Perovskite–Silicon Tandem Solar Cells," *Nature Nanotechnology* 17 (2022): 1214–1221.

19. A. Harter, K. Artuk, F. Mathies, et al., "Perovskite/Silicon Tandem Solar Cells Above 30% Conversion Efficiency on Submicron-Sized Textured Czochralski-Silicon Bottom Cells with Improved Hole-Transport Layers," *ACS Applied Materials & Interfaces* 16 (2024): 62817–62826, https://doi.org/10.1021/acsami.4c09264.

20. X. Luo, H. Luo, H. Li, et al., "Efficient Perovskite/Silicon Tandem Solar Cells on Industrially Compatible Textured Silicon," *Advanced Materials* 35 (2023): 2207883.

21. L. Mazzarella, Y. H. Lin, S. Kirner, et al., "Infrared Light Management Using a Nanocrystalline Silicon Oxide Interlayer in Monolithic Perovskite/Silicon Heterojunction Tandem Solar Cells with Efficiency above 25%," *Advanced Energy Materials* 9 (2019): 1803241.

22. A. Cruz, D. Erfurt, P. Wagner, et al., "Optoelectrical Analysis of TCO+Silicon Oxide Double Layers At The Front And Rear Side Of Silicon Heterojunction Solar Cells," *Solar Energy Materials and Solar Cells* 236 (2022): 111493.

23. P. Tockhorn, J. Sutter, R. Colom, et al., "Improved Quantum Efficiency by Advanced Light Management in Nanotextured Solution-Processed Perovskite Solar Cells," *ACS Photonics* 7 (2020): 2589–2600.

24. R. Santbergen, T. Meguro, T. Suezaki, G. Koizumi, K. Yamamoto, and M. Zeman, "GenPro$_4$ Optical Model for Solar Cell Simulation and Its Application to Multijunction Solar Cells," *IEEE Journal of Photovoltaics* 7 (2017): 919–926.

25. A. Fell, "A Free and Fast Three-Dimensional/Two-Dimensional Solar Cell Simulator Featuring Conductive Boundary and Quasi-Neutrality Approximations," *IEEE Transactions on Electron Devices* 60 (2013): 733–738.

26. Q. Jiang, Z. Chu, P. Wang, et al., "Planar-Structure Perovskite Solar Cells with Efficiency beyond 21%," *Advanced Materials* 29 (2017): 1703852.

27. J. F. Condeles, T. M. Martins, T. C. dos Santos, C. A. Brunello, M. Mulato, and J. M. Rosolen, "Fabrication and Characterization Of Thin Films of PbI_2 for Medical Imaging," *Journal of Non-Crystalline Solids* 338–340 (2004): 81–85.

28. G. Tumen-Ulzii, C. Qin, D. Klotz, et al., "Detrimental Effect of Unreacted PbI_2 on the Long-Term Stability of Perovskite Solar Cells," *Advanced Materials* 32 (2020): 1905035.

29. Y. Gao, H. Raza, Z. Zhang, W. Chen, and Z. Liu, "Rethinking the Role of Excess/Residual Lead Iodide in Perovskite Solar Cells," *Advanced Functional Materials* 33 (2023): 2215171.

30. J. Chang, Q. Zhou, Y. Wang, and W. Yan, "The Residual PbI_2 Paradox in Perovskite Solar Cells: Harnessing Excess Phase for Synergistic Performance-Stability Improvement," *Small* 22 (2026): 73477.

31. M. Stolterfoht, C. M. Wolff, J. A. Márquez, et al., "Visualization And Suppression Of Interfacial Recombination For High-Efficiency Large-Area Pin Perovskite Solar Cells," *Nature Energy* 3 (2018): 847–854.

32. U. Rau, "Reciprocity Relation Between Photovoltaic Quantum Efficiency And Electroluminescent Emission Of Solar Cells," *Physical Review B* 76 (2007): 085303.

33. C. Schinke, D. Hinken, J. Schmidt, K. Bothe, and R. Brendel, "Modeling the Spectral Luminescence Emission of Silicon Solar Cells and Wafers," *IEEE Journal of Photovoltaics* 3 (2013): 1038–1052.

34. C. Barugkin, T. Allen, T. K. Chong, T. P. White, K. J. Weber, and K. R. Catchpole, "Light Trapping Efficiency Comparison Of Si Solar Cell Textures Using Spectral Photoluminescence," *Optics Express* 23 (2015): A391.

35. O. Er-raji, M. A. A. Mahmoud, O. Fischer, et al., "Tailoring Perovskite Crystallization And Interfacial Passivation In Efficient, Fully Textured Perovskite Silicon Tandem Solar Cells," *Joule* 8 (2024): 2811–2833.

36. T. W. Gries, D. Regaldo, H. Koebler, et al., "Co-Doping Approach for Enhanced Electron Extraction to TiO2 for Stable Inorganic Perovskite Solar Cells," *Small Science* 5 (2025), 2400578, https://doi.org/10.1002/smsc.202400578.

37. I. Levine, A. Al-Ashouri, A. Musiienko, et al., "Charge Transfer Rates And Electron Trapping At Buried Interfaces Of Perovskite Solar Cells," *Joule* 5 (2021): 2915–2933.

38. A. Al-Ashouri, A. Magomedov, M. Roß, et al., "Conformal Monolayer Contacts With Lossless Interfaces For Perovskite Single Junction And Monolithic Tandem Solar Cells," *Energy & Environmental Science* 12 (2019): 3356–3369.

39. J. Warby, F. Zu, S. Zeiske, et al., "Understanding Performance Limiting Interfacial Recombination in pin Perovskite Solar Cells," *Advanced Energy Materials* 12 (2022): 2103567.

40. D. Abdel, J. Relle, T. Kirchartz, et al., "How Nanotextured Interfaces Influence The Electronics In Perovskite Solar Cells," *EES Solar* 2 (2026): 436.

41. A. Cruz, E. C. Wang, A. B. Morales-Vilches, et al., "Effect of Front TCO on the Performance Of Rear-Junction Silicon Heterojunction Solar Cells: Insights From Simulations And Experiments," *Solar Energy Materials and Solar Cells* 195 (2019): 339–345.

42. H. Sai, H. Jia, and M. Kondo, "Impact Of Front And Rear Texture Of Thin-Film Microcrystalline Silicon Solar Cells On Their Light Trapping Properties," *Journal of Applied Physics* 108 (2010): 044505.

43. R. Santbergen, M. R. Vogt, R. Mishima, et al., "Ray-Optics Study Of Gentle Non-Conformal Texture Morphologies For Perovskite/Silicon Tandems," *Optics Express* 30 (2022): 5608.

44. J. Keil, B. M. Cote, V. Chandrasekaran, A. Los, and V. E. Ferry, "Minimizing Roughness Induced Optical Losses for a Four-Terminal Cd Te/Si Tandem Solar Cell," *PRX Energy* 2 (2023): 023004.

16163028, 2026, 76, Downloaded from https://advanced.onlinelibrary.wiley.com/doi/10.1002/adfm.77815 by Helmholtz-Zentrum Berlin Für, Wiley Online Library on [10/11/2026]. See the Terms and Conditions (https://onlinelibrary.wiley.com/terms-and-conditions) on Wiley Online Library for rules of use; OA articles are governed by the applicable Creative Commons License

45. Y. Yun, K. J. Prince, S. Berwig, et al., "Triple-Junction All-Perovskite Solar Cells With Self-Assembling Hole Contacts In All Subcells," *Joule* (2026): 102575, https://doi.org/10.1016/j.joule.2026.102575.

46. X. Liao, X. Xiang, and X. Zeng, "Modeling Analyses For Current Matching In Tandem Solar Cells," in IEEE International Conference on Electro-Information Technology (IEEE, 2013), 1–4.

47. J. Wen, H. Hu, C. Chen, et al., "Present Status Of And Future Opportunities For All-Perovskite Tandem Photovoltaics," *Nature Energy* 10 (2025): 681–696.

48. A. R. Bowman, F. Lang, Y. H. Chiang, et al., "Relaxed Current Matching Requirements in Highly Luminescent Perovskite Tandem Solar Cells and Their Fundamental Efficiency Limits," *ACS Energy Letters* 6 (2021): 612–620.

49. Z. Yang, Z. Yu, H. Wei, et al., "Enhancing Electron Diffusion Length In Narrow-Bandgap Perovskites For Efficient Monolithic Perovskite Tandem Solar Cells," *Nature Communications* 10 (2019): 4498.

50. Z. Yu, Z. Yang, Z. Ni, et al., "Simplified Interconnection Structure Based on C60/SnO_{2-x} for All-Perovskite Tandem Solar Cells," *Nature Energy* 5 (2020): 657–665.

51. M. R. Fitzsimmons, B. Roose, Y. Han, et al., "Optimized Graphene-Oxide-Based Interconnecting Layer in All-Perovskite Tandem Solar Cells," *ACS Energy Letters* 10, no. (2) (2025): 713–725.

52. S. Kim, D. Im, Y. Yun, et al., "Stabilizing Wide-Bandgap Perovskite with Nanoscale Inorganic Halide Barriers for Next-Generation Tandem Technology," *Advanced Enenrgy Materials* 15 (2025): 2404366, https://doi.org/10.1002/aenm.202404366.

53. H. Kumar Raut, V. Anand Ganesh, A. Sreekumaran Nair, and S. Ramakrishna, "Interface Design To Improve Stability Of Polymer Solar Cells For Potential Space Applications," *Energy & Environmental Science* 4 (2011): 4917.

54. J. Heo, A. S. Hock, and R. G. Gordon, "Low Temperature Atomic Layer Deposition of Tin Oxide," *Chemistry of Materials* 22 (2010): 4964–4973.

55. D. Choi and J. S. Park, "Highly Conductive SnO_2 Thin Films Deposited By Atomic Layer Deposition Using Tetrakis-Dimethyl-Amine-Tin Precursor And Ozone Reactant," *Surface and Coatings Technology* 259 (2014): 238–243.

56. J. A. Raiford, C. C. Boyd, A. F. Palmstrom, et al., "Enhanced Nucleation of Atomic Layer Deposited Contacts Improves Operational Stability of Perovskite Solar Cells in Air," *Advanced Energy Materials* 9 (2019): 1902353.

57. L. Yao, B. Chen, Z. Li, et al., "Atomic Layer Deposited Tin Oxide Buffer Layer via Layer-by-layer Growth for Efficient Semitransparent Perovskite Solar Cells," *Small* 21 (2025): 02206.

58. A. Kasikov, J. Aarik, H. Mändar, M. Moppel, M. Pärs, and T. Uustare, "Refractive Index Gradients in TiO_2 Thin Films Grown By Atomic Layer Deposition," *Journal of Physics D: Applied Physics* 39 (2005): 54–60.

59. D. E. Jung, I. R. Howell, V. J. Einck, et al., "Refractive Index Tuning of All-Inorganic TiO2 Nanocrystal-Based Films and High Aspect Ratio Nanostructures Using Atomic Layer Deposition: Implications for High-Throughput Fabrication of Metalenses," *ACS Applied Nano Materials* 6 (2023): 2009.

60. E. Köhnen, M. Jošt, A. B. Morales-Vilches, et al., "Highly Efficient Monolithic Perovskite Silicon Tandem Solar Cells: Analyzing The Influence Of Current Mismatch On Device Performance," *Sustainable Energy Fuels* 3 (2019): 1995.

61. E. Yablonovitch and G. D. Cody, "Intensity Enhancement In Textured Optical Sheets For Solar Cells," *IEEE Transactions on Electron Devices* 29 (1982): 300–305.

62. D. Zhang, T. Wu, B. Li, et al., "Iceberg-Like Pyramids In Industrially Textured Silicon Enabled 33% Efficient Perovskite-Silicon Tandem Solar Cells," *Nature Communications* 16 (2025): 7331.

63. M. Roß, S. Severin, M. B. Stutz, et al., "Co-Evaporated Formamidinium Lead Iodide Based Perovskites With 1000 h Constant Stability For Fully Textured Monolithic Perovskite/Silicon Tandem Solar Cells," *Advanced Energy Materials* 11 (2021): 2101460.

64. F. Sahli, J. Werner, B. A. Kamino, et al., "Fully Textured Monolithic Perovskite/Silicon Tandem Solar Cells With 25.2% Power Conversion Efficiency," *Nature Materials* 17 (2018): 820–826.

65. H. Winarto, J. Sutter, P. Tockhorn, et al., "Periodic Inverted Micropyramids for Optically Optimized Fully Textured Solution-Processed Perovskite Solar Cells," *Solar RRL* 9 (2025): 202500613.

66. L. M. van der Poll, N. van Silfhout, J. Nespoli, et al., "Additive-Free Sequential Thermal Evaporation of Near-Intrinsic Pb-Sn Perovskites," *Small Methods* 9 (2025): 2401246.

67. L. M. van der Poll, M. C. Díaz, R. K. Boekhoff, et al., "Interplay Of Diffusion And Crystallization In Sequentially Evaporated Lead Tin Perovskites," *EES Solar* (2026), https://doi.org/10.1039/d6el00044d.

68. Z. C. Holman, M. Filipič, A. Descoeudres, et al., "Infrared Light Management In High-Efficiency Silicon Heterojunction And Rear-Passivated Solar Cells," *Journal of Applied Physics* 113 (2013): 013107.

69. Y. Wang, R. Lin, X. Wang, et al., "Oxidation-Resistant All-Perovskite Tandem Solar Cells In Substrate Configuration," *Nature Communications* 14 (2023): 1819.

70. W. Yang, Y. Zhang, C. Xiao, J. Yang, and T. Shi, "A Review Of Encapsulation Methods And Geometric Improvements Of Perovskite Solar Cells And Modules For Mass Production And Commercialization," *Nano Materials Science* 7 (2025): 790–809.

71. X. Huang, D. Xia, Q. Xie, et al., "Supramolecular Force-Driven Non-Fullerene Acceptors As An Electron-Transporting Layer For Efficient Inverted Perovskite Solar Cells," *Nature Communications* 16 (2025): 1626.

72. K. Feng, G. Wang, Q. Lian, et al., "Non-Fullerene Electron-Transporting Materials For High-Performance And Stable Perovskite Solar Cells," *Nature Materials* 24 (2025): 770–777.

73. Z. Chen, B. Turedi, A. Y. Alsalloum, et al., "Single-Crystal MAPbI3 Perovskite Solar Cells Exceeding 21% Power Conversion Efficiency," *ACS Energy Letters* 4 (2019): 1258.

74. V. Yeddu, K. Almasabi, Y. Xu, et al., "In-Situ Self-Assembly Of Hole Transport Monolayer During Crystallization For Efficient Single-Crystal Perovskite Solar Cells," *Nature Communications* 16 (2025): 7245.

75. L. Chen, Y. Y. Tan, Z. X. Chen, et al., "Toward Long-Term Stability: Single-Crystal Alloys of Cesium-Containing Mixed Cation and Mixed Halide Perovskite," *Journal of the American Chemical Society* 141 (2019): 1665–1671.

76. Z. Chang, Z. Lu, W. Deng, et al., "Narrow-Bandgap Sn–Pb Mixed Perovskite Single Crystals For High-Performance Near-Infrared Photodetectors," *Nanoscale* 15 (2023): 5053–5062.

77. M. Jošt, L. Kegelmann, L. Korte, and S. Albrecht, "Monolithic Perovskite Tandem Solar Cells: A Review Of The Present Status And Advanced Characterization Methods Toward 30% Efficiency," *Advanced Energy Materials* 10 (2020): 1904102.

78. M. Daub and H. Hillebrecht, "Tailoring the Band Gap in 3D Hybrid Perovskites by Substitution of the Organic Cations: $(CH_3NH_3)_{1-2y}$ $(NH_3(CH_2)_2\ NH_3)_{2y}$ $Pb_{1-y}\ I_3$ $(0\leq y \leq 0.25)$," *Chemistry – A European Journal* 24 (2018): 9075–9082.

Supporting Information

Additional supporting information can be found online in the Supporting Information section.

Supporting File: adfm77815-sup-0001-SuppMat.docx.

16163028, 2026, 76, Downloaded from https://advanced.onlinelibrary.wiley.com/doi/10.1002/adfm.77815 by Helmholtz-Zentrum Berlin Für, Wiley Online Library on [10/11/2026]. See the Terms and Conditions (https://onlinelibrary.wiley.com/terms-and-conditions) on Wiley Online Library for rules of use; OA articles are governed by the applicable Creative Commons License